RETINAL DISEASE

Calcified nodules in retinal drusen are associated with disease progression in age-related macular degeneration

Anna C. S. Tan[1,2,3,4]*, Matthew G. Pilgrim[5,6]*, Sarah Fearn[7], Sergio Bertazzo[8], Elena Tsolaki[8], Alexander P. Morrell[9], Miaoling Li[10], Jeffrey D. Messinger[10], Rosa Dolz-Marco[1,2], Jianqin Lei[11], Muneeswar G. Nittala[11], Srinivas R. Sadda[11,12], Imre Lengyel[5,13]†‡, K. Bailey Freund[1,2,14]‡, Christine A. Curcio[10]‡

Drusen are lipid-, mineral-, and protein-containing extracellular deposits that accumulate between the basal lamina of the retinal pigment epithelium (RPE) and Bruch's membrane (BrM) of the human eye. They are a defining feature of age-related macular degeneration (AMD), a common sight-threatening disease of older adults. The appearance of heterogeneous internal reflectivity within drusen (HIRD) on optical coherence tomography (OCT) images has been suggested to indicate an increased risk of progression to advanced AMD. Here, in a cohort of patients with AMD and drusen, we show that HIRD indicated an increased risk of developing advanced AMD within 1 year. Using multimodal imaging in an independent cohort, we demonstrate that progression to AMD was associated with increasing degeneration of the RPE overlying HIRD. Morphological analysis of clinically imaged cadaveric human eye samples revealed that HIRD was formed by multilobular nodules. Nanoanalytical methods showed that nodules were composed of hydroxyapatite and that they differed from spherules and BrM plaques, other refractile features also found in the retinas of patients with AMD. These findings suggest that hydroxyapatite nodules may be indicators of progression to advanced AMD and that using multimodal clinical imaging to determine the composition of macular calcifications may help to direct therapeutic strategies and outcome measures in AMD.

INTRODUCTION

Globally, age-related macular degeneration (AMD) is a prevalent cause of legal blindness in the elderly (*1*). Although effective therapies exist for the neovascular form of advanced AMD (*2*), there is no approved treatment for geographic atrophy (GA) (*3*), the advanced form of AMD defined by focal atrophy of the retinal pigment epithelium (RPE) in the setting of extracellular deposits called drusen. Drusen, which occur early in AMD, are lipid-containing (*4*–*8*), mineral-containing (*9*, *10*), and protein-containing (*11*–*14*) extracellular deposits between the basal lamina of the RPE and Bruch's membrane (BrM) (*15*, *16*). RPE cells support overlying photoreceptors and underlying choroidal vasculature, of which BrM, a layered extracellular matrix, is the innermost component.

Clear ocular optics and sophisticated cellular-level clinical imaging techniques allow detailed study of AMD microarchitecture in vivo (*17*, *18*). Indicators of disease severity and therapeutic efficacy might help the design and evaluation of clinical trials and the identification of targetable biological processes to both prevent progression and treat advanced AMD. Imaging methodologies based on high-speed optical coherence tomography (OCT) are being used to define indicators that predict an increased risk of progression in eyes with intermediate AMD (*19*). Three distinctive OCT reflectivity signatures appear in eyes with GA: (i) small hyperreflective dots within drusen (*20*), (ii) heterogeneous internal reflectivity within drusen (HIRD) (*21*, *22*), and (iii) hyperreflective lines near BrM (*23*, *24*). Of these, HIRD has been shown to be associated with increased risk for progression to advanced AMD (*21*). The composition of HIRD and why they are hyporeflective are not yet defined.

At least three forms of calcifications (mineral depositions) capable of generating OCT reflectivity have been identified in AMD-affected tissues by various techniques (table S1), including light microscopy for refractility, histochemical stains for phosphate and hydroxyapatite (HAP), and elemental and diffraction analysis for minerals. Drusen contain small spherules that are refractile, histochemically positive for phosphates and HAP (*25*, *26*), and exhibit HAP-like patterns when interrogated by synchrotron micro–x-ray diffraction (*9*, *10*). BrM plaques contain phosphate by histochemistry (*27*) and calcium by elemental analysis (*26*, *28*), but in vivo reflectivity characteristics are unknown. Nodules are large, refractile, multilobed (*20*) structures that are positive for phosphates (*29*). Nodules currently lack both a definitive mineral composition and an imaging signature. On the basis of spherules and BrM plaques, we expect that nodules also contain calcium phosphate.

Materials science has contributed important new concepts about the composition and formation of early bone development, ectopic calcification in cardiovascular disease (*30*, *31*), and HAP spherules in drusen (*20*). We reasoned that this approach could also reveal composition and suggest formative processes of HIRD and plaques.

[1]Vitreous Retina Macula Consultants of New York, New York, NY 10022, USA. [2]LuEsther T. Mertz Retinal Research Center, Manhattan, Eye, Ear and Throat Hospital, New York, NY 10075, USA. [3]Singapore National Eye Center/Singapore Eye Research Institute Singapore, Singapore 168751, Singapore. [4]Duke-NUS Singapore, Singapore 168751, Singapore. [5]UCL Institute of Ophthalmology, 11-43 Bath Street, London EC1V 9EL, UK. [6]Division of Biomaterials and Tissue Engineering, UCL Eastman Dental Institute, University College London, London WC1X 8LD, UK. [7]Department of Materials, Imperial College London, London SW7 2AZ, UK. [8]Department of Medical Physics and Biomedical Engineering, University College London, Malet Place Engineering Building, London WC1E 6BT, UK. [9]Material Physics, Aston University, Aston Express Way, Birmingham B4 7ET, UK. [10]Department of Ophthalmology, School of Medicine, University of Alabama at Birmingham, Birmingham, AL 32594-0019, USA. [11]Doheny Image Reading Center, Doheny Eye Institute, Los Angeles, CA 90033, USA. [12]Department of Ophthalmology, David Geffen School of Medicine at UCLA, Los Angeles, CA 90095, USA. [13]Centre for Experimental Medicine, School of Medicine, Dentistry and Biomedical Science, Queen's University Belfast, Belfast BT9 7BL, UK. [14]Department of Ophthalmology, New York University Langone School of Medicine, New York, NY 10016, USA.
*These authors contributed equally to this work.
†Corresponding author. Email: i.lengyel@qub.ac.uk
‡Co-senior authors.

Using a combination of clinical, histopathologic, and molecular imaging techniques, we determined that the HIRD progression indicator is a nodule, that is, a crystalline calcium phosphate mineral molecularly distinct from both spherules and plaques. On the basis of our results, we propose that a multimodal imaging staging system evaluating the composition of drusen might be useful for determining the risk of progression in AMD.

RESULTS

Multimodal imaging appearance of potentially calcified structures

To define and contextualize OCT signatures in human patients with AMD, we used multimodal clinical imaging of 97 HIRD in cohort 1. Cohort 1 was composed of 21 eyes (HIRD per eye, mean, 4.6; range, 1 to 15) of 17 patients with AMD (6 men and 11 women; age at baseline, 75.9 ± 10.4 years; range, 58 to 94 years) for a mean of 6.17 years (range, 3.2 to 7.5 years; mean number of consecutive OCT scans per eye, 22.9; range, 10 to 62; total of 1198 B-scans, original data are in dataset S1).

HIRD were identified on OCT within RPE elevations by reference to previous descriptions. They were occasionally associated with hyperreflective interior substructures (Fig. 1 A, red arrow), nonrefractile appearance on color fundus photography (CFP) (Fig. 1B, red arrow), isoautofluorescent in an area of confluent hypoautofluorescence on fundus autofluorescence (FAF) (Fig. 1C, red arrow), and nonreflective on near-infrared reflectance (NIR) imaging (Fig. 1D, red arrow). A thickened hyperreflective cap (Fig. 1A, pink arrowhead) that is nonrefractile on CFP (Fig. 1B, pink arrowhead) appears mildly hypoautofluorescent with a hyperautofluorescent ring on FAF (Fig. 1C, pink arrowhead) and is mildly hyperreflective on NIR (Fig. 1D, pink arrowhead). Hyperreflective dots within HIRD (Fig. 1A, green circle) are visible as glistening dots on CFP (Fig. 1B, green circle), occasionally hidden by a hyperreflective cap (Fig. 1A, pink arrowhead), undetectable on FAF (Fig. 1C, green circle), and hyperreflective on NIR (Fig. 1D, green circle). Hyperreflective lines that are parallel to and sometimes indistinguishable from BrM (Fig. 1A, blue arrowhead) are glistening on CFP (Fig. 1B, blue arrowhead), hypoautofluorescent on FAF (Fig. 1C, blue arrowhead), and highly reflective on NIR (Fig. 1D, blue arrowhead). During the follow-up period, the number of lesions visible on CFP, NIR, and FAF all increased ($P < 0.05$, Fisher's exact test; fig. S1). Together, HIRD and the overlying reflective caps were independently described in OCT as hyperreflective pyramidal structures (*22*) and conical-type drusen (*32*).

HIRD association with progression to advanced AMD

To understand the prognostic potential of HIRD for advanced AMD and determine whether the original finding of progression risk (*21*) could be replicated, we performed a 12-month-long longitudinal observation study. A total of 138 eyes from 138 patients in cohort 2 (mean age, 80.2 years ± 7.8; range, 63 to 96 years; 55 males and 76 females) (original data are detailed in dataset S2), with intermediate AMD and sequential OCT data, were analyzed for the presence of HIRD on dense-volume OCT scans. Among these 138 eyes, 62 (45%) had evidence of at least one HIRD on OCT. Fifty-five (40%) progressed to advanced AMD (defined as neovascular AMD or GA) within the next 12 months, including 33 that progressed to GA only, 14 that progressed to choroidal neovascularization (CNV) only, and 8 that progressed to both atrophy and CNV. HIRD were significantly and independently associated with progression to advanced AMD at 12 months with an odds ratio of 6.36 (95% confidence interval, 2.99 to 13.53; $P < 0.001$), suggesting that HIRD might have prognostic value for neovascular AMD and GA.

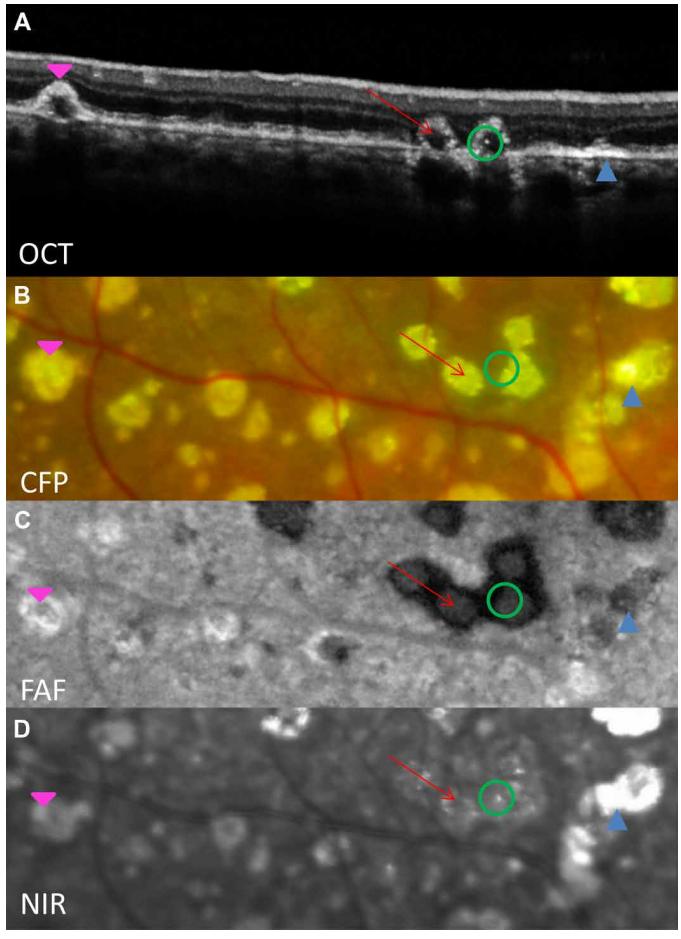

Fig. 1. Multimodal imaging of three types of calcified structures associated with advanced AMD. HIRD, reflective dots, and plaques seen on (**A**) OCT, (**B**) CFP, (**C**) FAF, and (**D**) NIR. HIRD with a hyporeflective core (red arrow) and a hyperreflective cap (pink arrowhead), hyperreflective dots (green circle), and hyperreflective areas (blue arrowhead) are indicated.

Imaging-histology correlation of HIRD

To link OCT imaging characteristics with molecular analysis, we correlated OCT with histology in eyes of deceased eye donors. Case 1 was the left eye of an 86-year-old woman with GA, recovered 4 months after the last clinic visit (Fig. 2, A and B). HIRD on OCT corresponded to a multilobular nodule amid typical soft druse contents, overlaid by RPE and thick basal laminar deposit (BLamD; thickened RPE basement membrane) (Fig. 2, C and D). Case 2 was the left eye of a clinically undocumented donor with macroscopically visible GA that was imaged with ex vivo OCT (Fig. 2, E and F). HIRD corresponded to a central nodule surrounded by proteinaceous material, covered by thin BLamD, in the absence of RPE (Fig. 2G) and photoreceptors (Fig. 2H).

To derive a plausible pathogenic sequence for HIRD (Fig. 3), we examined images from an online resource for AMD histopathology

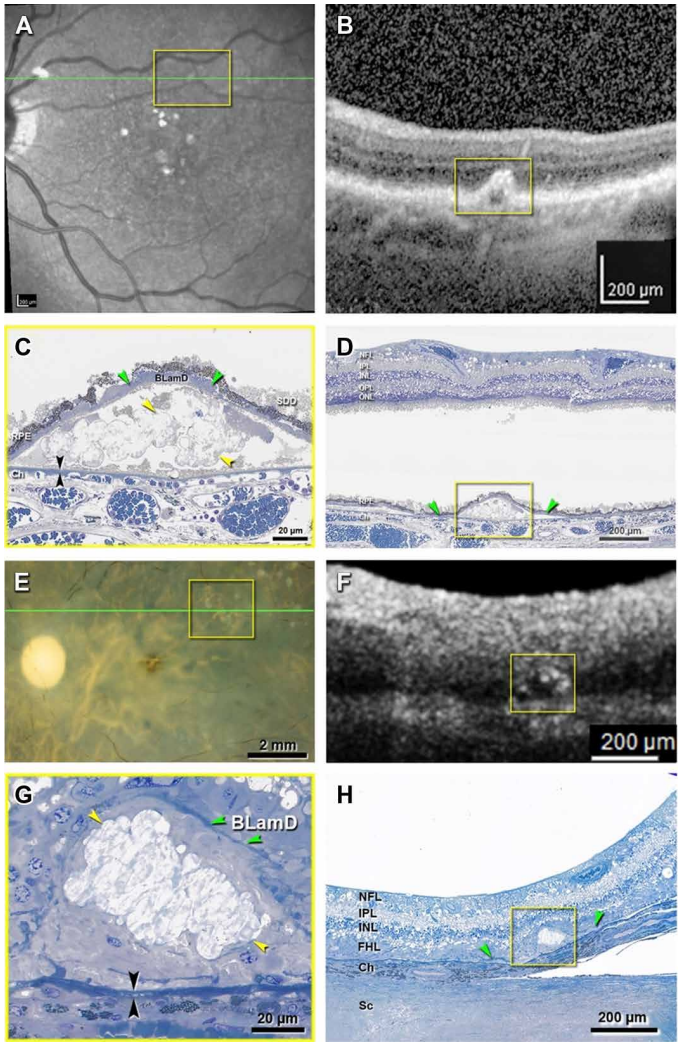

Fig. 2. Imaging of HIRD by OCT and nodules by histology. (**A** to **D**) Eye of an 86-year-old white female with GA imaged in vivo 4 months before death. (A) NIR image shows translucent large drusen. Green line, level of OCT scan in (B). Yellow frame, druse on (B) to (D). (B) OCT image showing HIRD (yellow frame). (C) Druse corresponding to the HIRD. Large refractile nodules are surrounded by lipid-rich soft druse material (gray). SDD, subretinal drusenoid deposits. (D) Panoramic light microscopy. The HIRD of (B) and the druse are at the same distance from the optic nerve head, as determined by comparing corresponding OCT scans and histology at the same dimensions. (**E** to **H**) Eye of a 94-year-old white female with GA imaged ex vivo. (E) CFP shows refractile drusen in the superior temporal quadrant. Green line, level of OCT scan in (F). (F) Yellow frame denotes an HIRD. (G) Calcific nodules are surrounded by processes of Müller cells. Overlying BLamD is thin and fragmented. (H) Context of calcified druse showing degeneration of outer retina including gliotic Henle fiber layer and absent photoreceptors. Submicrometer epoxy resin sections of osmium tannic acid paraphenylenediamine post-fixed specimens stained in toluidine blue. Separation of retina from RPE (B) and choroid from sclera (H) is artifactual. NFL, nerve fiber layer; IPL, inner plexiform layer; INL, inner nuclear layer; HFL, Henle fiber layer; OPL, outer plexiform layer; ONL, outer nuclear layer; BLamD, basal laminar deposit (a thickening of basement membrane material between the RPE and its basement lamina); Ch, choroid; Sc, sclera. Yellow arrowheads, calcific nodules; green arrowheads, BLamD; black arrowheads, BrM.

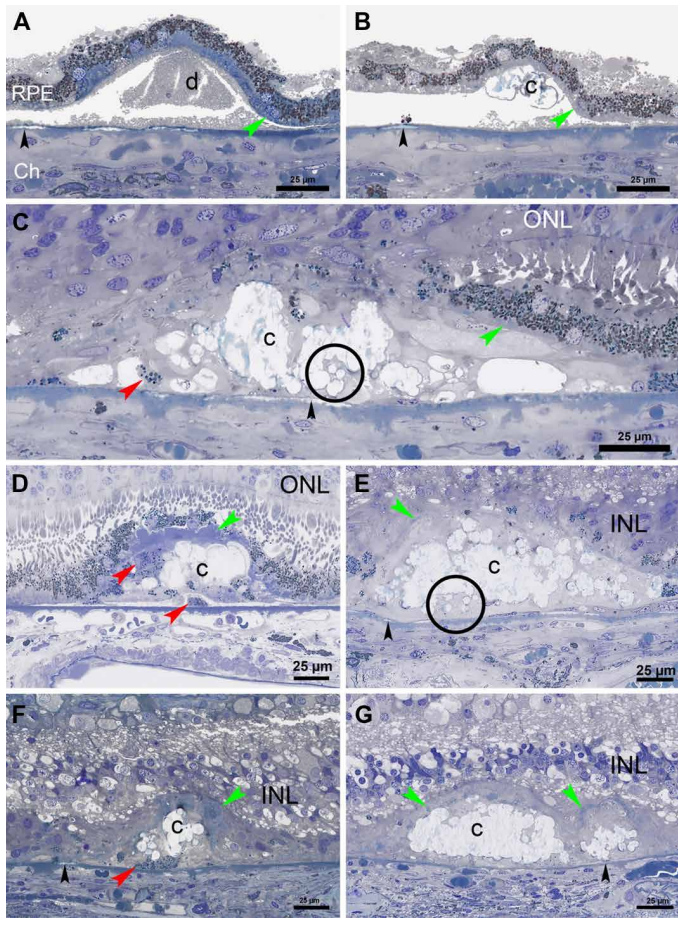

Fig. 3. Histological variants of calcific nodule formation and RPE degeneration in GA. (**A**) Small soft druse (d) containing lipoprotein-derived debris (artifactually fractured) and intact overlying RPE. (**B**) Small soft druse with partial contents, refractile nodules, and intact overlying RPE. (**C**) Calcific nodules and spherules and RPE-derived granule aggregates, with partial covering of RPE and photoreceptors, and lacking BLamD. (**D**) Druse with calcific nodules and nucleated "subducted" RPE with thick overlying BLamD and nearly complete coverage by RPE. (**E**) Calcific nodules with very thin BLamD and no RPE. (**F**) Calcific nodules with thin BLamD and subducted RPE. (**G**) Calcific nodules are found with thin overlying BLamD. Submicrometer epoxy resin sections of osmium tannic acid paraphenylenediamine post-fixed specimens stained in toluidine blue. Green arrowheads, BLamD; c, calcific nodule; black circle, calcific spherules; black arrowheads, calcification within BrM; red arrowheads, RPE/RPE-derived material as indicated.

(http://projectmacula.cs.uab.edu/) (n = 139; 26 with early AMD, 13 with GA, 40 with neovascular AMD, 52 with healthy maculas, and 8 with other or unknown characteristics; mean age, 82.8 years; SD, 8.4 years; all white, 89 females and 50 males). We found that large nodules and isolated RPE cells appeared only within the original lipidic contents of soft drusen, often surrounded by a fibrous material (Fig. 3, A and B). As RPE coverage gradually decreased (Fig. 3, C and D), and BLamD persisted after RPE loss (Fig. 3, E to G), contents of individual drusen were replaced by nodules, as previously described (Fig. 3, C to G) (*33*). Drusen in Fig. 3 (C to G) have both nodules and spherules, always distinct from BrM. In contrast, BrM has refractile plaques distinct from the structures in drusen (Figs. 2G and 3, A to G). Together, this analysis suggests that nodules might play a major role in HIRD.

Composition of nodules, spherules, and BrM plaques

To investigate nodule composition, we used scanning electron microscopy (SEM), energy-dispersive x-ray (EDX) spectroscopy,

HAP-specific fluorescent staining, secondary ion mass spectrometry (SIMS), and synchrotron x-ray fluorescence and transmission electron microscopy–selected-area electron diffraction (TEM-SAED). Table S2 shows that all techniques were applied to samples of at least two different donors.

We analyzed two histologically verified AMD cases. The first AMD case presented a serous RPE detachment and RPE atrophy and exhibited cloud-like pearly drusen and conventional soft drusen (fig. S2) (*34*). The second AMD case had refractile nodules within microdissected macular soft drusen that were also amenable to analysis (*35*). In both cases, nodules, spherules, and plaques were first examined using SEM. Nodules (Fig. 4A and fig. S3) and spherules (Fig. 4B) were readily visible on scanning electron micrographs because of their distinct morphology; however, plaques were not (Fig. 4, C and D). Plaques were identifiable only by backscattered SEM, which showed dense material within BrM, likely mineralization (fig. S4).

Nodules (table S2) were subsequently examined with EDX spectroscopy. One discrete peak corresponding to phosphorus (P) and calcium (Ca) were clearly identifiable on spectra obtained from spherules (Fig. 4L), plaques (Fig. 4M), and nodules (Fig. 4K). This suggests that all three lesions are composed of an inorganic calcium phosphate. Peaks corresponding to carbon (C), oxygen (O), and sodium (Na) emanating from the mineralized lesions and from the surrounding organic soft tissues were also present (Fig. 4, K to M). A small discrete peak for magnesium (Mg) was also present on spectra from spherules and plaques; however, this peak was absent for nodules (Fig. 4, K to M). To confirm Ca and P as major components, we mapped the Ca and P x-ray emissions. Ca and P were always enriched within nodules, spherules, and plaques compared to the surrounding tissues [Fig. 4, E and H (nodule); Fig. 4, F and I (spherule); and Fig. 4, G and J (BrM plaque)]. Macular tissue with nodules, previously interrogated by ex vivo color imaging (*26*), was also investigated with microfocus synchrotron x-ray fluorescence, and we confirmed the presence of Ca (fig. S5C).

Isolated nodules etched of resin and sectioned to 2-μm thickness were also characterized using time-of-flight–SIMS (TOF-SIMS) (table S2). Typical ionic signatures including 39.9, 55.9, 102.9, 158.9, 174.9, and 230.8 mass/charge ratio corresponding to $[Ca^+]$, $[CaO^+]$, $[CaPO_2^+]$, $[Ca_2PO_3^+]$, $[Ca_2PO_4^+]$, and $[Ca_3PO_5^+]$, respectively, were detected. It was previously reported that these signatures indicate inorganic HAP (*36*), suggesting that nodules also contain this calcium phosphate compound. Molecular mapping of $[Ca^+]$, $[CaPO_2^+]$, and the sum of all detected CaP signatures confirmed the presence of calcium phosphate within nodules (fig. S6).

Calcific lesions stained with the apatite-specific bioimaging agent OsteoSense 680EX were shown using confocal fluorescence microscopy (table S2). Nodules were heterogeneously stained, with crusts staining intensely (Fig. 4N, arrowhead). A previously reported, (*9*, *10*) some spherules appeared to have a hollow core of apatite (Fig. 4O). Also, plaques stained with OsteoSense 680EX (Fig. 4P). These results suggest that nodules, spherules, and plaques were all composed of apatite.

The detection of secondary ions associated with HAP such as $[Ca^+]$, $[CaO^+]$, $[CaPO_2^+]$, $[Ca_2PO_3^+]$, $[Ca_2PO_4^+]$, and $[Ca_3PO_5^+]$ (*36*), as well as positive OsteoSense 680EX staining suggested that HAP could be the major constituent of nodules. To explore the phases of calcium phosphate present in nodules, spherules, and plaques, we used TEM-SAED on samples sectioned by a focused ion beam.

Each deposit was first characterized by TEM (Fig. 5, A to I). As observed by light microscopy, nodules had numerous lobes, ~1 to 20 μm in diameter (Fig. 5, A and D), each with a distinct electron-dense outer crust and a less electron-dense inner core (Fig. 5, A and D). Like nodules, spherules were also electron dense with an inner core and a distinct outer shell (Fig. 5, B and E). In contrast to lobular or spherical deposition in nodules and spherules, respectively, calcium phosphate deposition in BrM plaques appear as disordered and crosshatched crystal needles (Fig. 5, C and F).

Subsequently, the calcium phosphate phases forming nodules, spherules, and BrM plaques were determined using SAED (Fig. 5, G to I). SAED produces diffractions rings that represent the distance (d-spacing or interplanar) between planes of atoms within a crystal lattice. These can be used to identify the mineral phase of a sample (*37*). Diffraction patterns obtained from nodules indicated a polycrystalline material composed of numerous unorganized crystals (Fig. 5G). Diffraction rings including (002), (300), (211), and (006) (*37*) confirmed that nodules were composed of HAP (table S3). Spherules are diffracted as a single crystal producing a spot pattern correlating to (010) zone axes of whitlockite (Fig. 5H). In contrast, BrM plaques produced diffuse rings, indicating the presence of an amorphous material with very low crystallinity (Fig. 5I). A diffuse ring encompassing multiple diffraction rings characteristic of apatite was detected (Fig. 5I).

DISCUSSION

Already a powerful tool to diagnose retinal disease, monitor progression, and provide end points for clinical trials (*38*), multimodal OCT-based clinical imaging can help define molecular pathogenesis if linked to the composition of visualized structures. Herein, we replicate and extend previous findings that HIRDs associate with progression to advanced AMD by applying the same imaging criteria to an independent cohort. Furthermore, we use histology, multimodal clinical imaging, and high-resolution molecular imaging to show that HIRDs are sprawling polycrystalline HAP nodules, distinctly different from the restricted sized spherules in drusen.

We propose a previously unidentified four-stage pathway for druse progression to HIRD by longitudinal multimodal clinical imaging (fig. S7). Variation A has less, and variation B has more, overlying BLamD, and similar trends were seen in both (fig. S8 and table S1). Stage 1: Druse under intact RPE and a thin layer of BLamD. Druse contents are homogeneously and moderately hyperreflective, without evidence of a hyporeflective core. HAP spherules (*10*) are undetectable because of shadowing by the RPE (*20*), the continuity of which is confirmed by FAF. Stage 2A: A hyporeflective core representing a nodule under intact RPE and surrounded by hyperreflective dots. Within overlying retina, hyperreflective foci (migrating RPE) (*39*) are visible. Stage 3A: Focal loss of RPE, visible on OCT as disruption, and thinning of the hyperreflective RPE–basal lamina band, gradually exposing the druse interior, which is reduced in volume. RPE loss is indicated by central hypoautofluorescence within a hyperautofluorescent border. Stage 4A: Complete loss of RPE overlying the nodule-filled druse, signified by absent FAF signal and a thin hyperreflective border of persistent BLamD. Relative to variation A, variation B exhibited less refractility on CFP, more hyperautofluorescence, and less hyperreflectivity on NIR (fig. S7). Most HIRD lesions were observed at stages 2 and 3 (figs. S1 and S8).

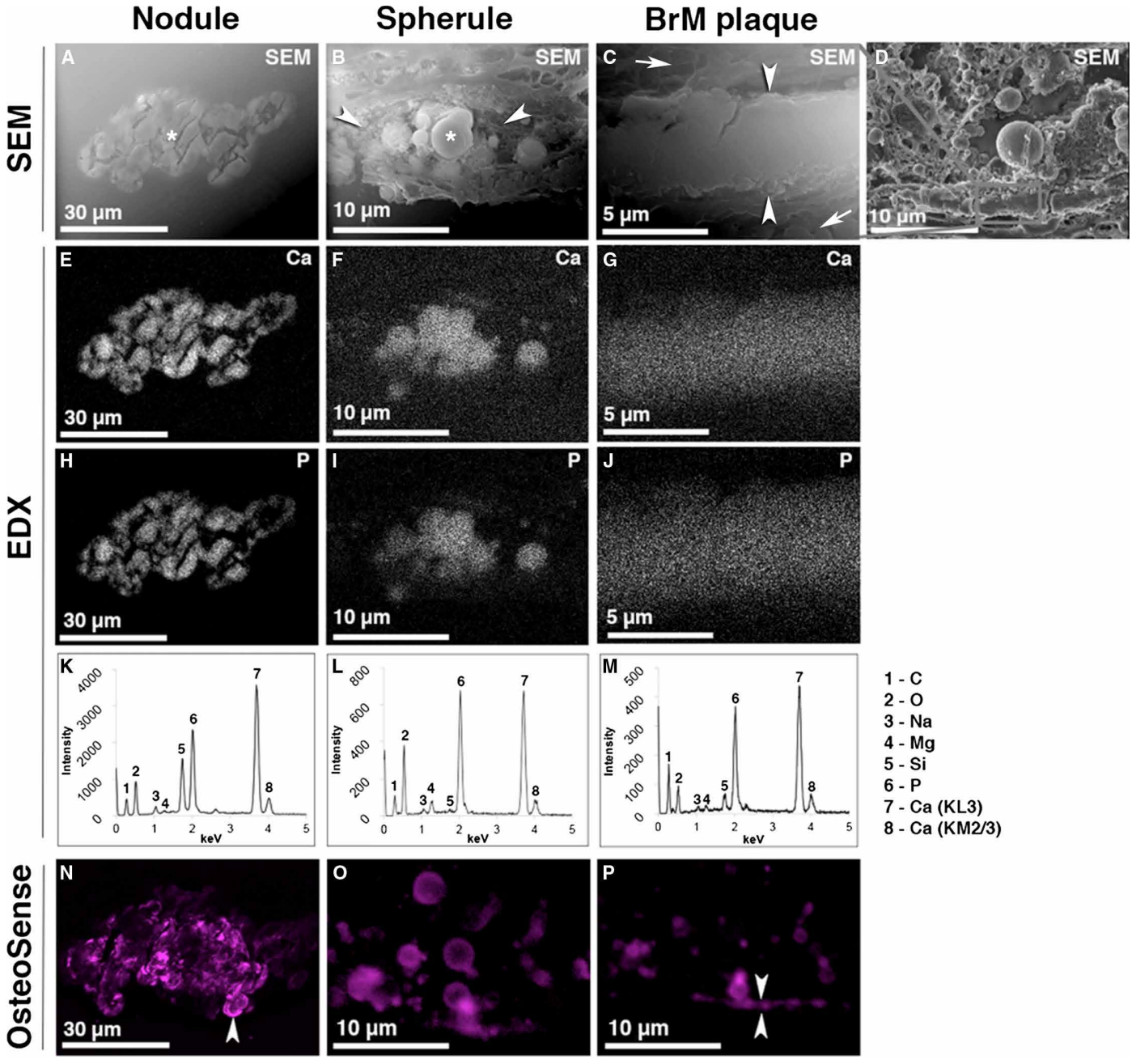

Fig. 4. SEM and EDX spectroscopy of nodules, spherules, and plaques. (**A** to **D**) High-magnification electron micrographs of calcific lesions. (A) An isolated nodule (asterisk) is composed of lobed units ~1 to 5 µm in diameter. Cracks present on the nodule surface were formed during sectioning. (B) Spherules (asterisk) about 0.5 to 5.0 µm in diameter were located between the basal lamina of the RPE and the inner collagenous layer of BrM, along with extracellular material (arrowheads). (C) Plaques (arrowheads), tens of micrometers in length and with cracks suggestive of mineralization, appeared visually similar to nonmineralized BrM. Arrows indicate surrounding tissues. (**E** to **J**) Elemental maps of nodules, spherules, and plaques generated using EDX spectroscopy. (E to G) X-ray emission maps specific to calcium. (H to J) X-ray emission maps specific to phosphate. (**K** to **M**) Representative EDX spectra of x-ray emissions for nodules, spherules, and plaques. (**N** to **P**) HAP-specific staining confirmed the presence of apatite in nodules, spherules, and plaques (arrowheads delimit the BrM).

We further propose (fig. S7) that in the presence of high overall extracellular calcium concentration, higher extracellular magnesium concentration and an acidic pH might promote spherule formation, whereas a lower magnesium concentration and neutral pH might promote nodule formation, as elaborated below. We suggest that the sub–RPE–basal lamina (BL) space transforms to a nodule-promoting environment by decreased release of Mg^{2+} as RPE cells die or migrate anteriorly atop the drusen (*40*), therefore suggesting that HIRD might be indicators of RPE in its agonal state. This interpretation is supported by focal HIRD-associated hypoautofluorescence (fig. S7). Thus, progression risk might be conferred not so much by HIRD themselves but by what they signify about RPE health.

Refractile drusen, appearing on ophthalmoscopy and CFP as glistening with reflective dots, were called "calcified" on the basis of

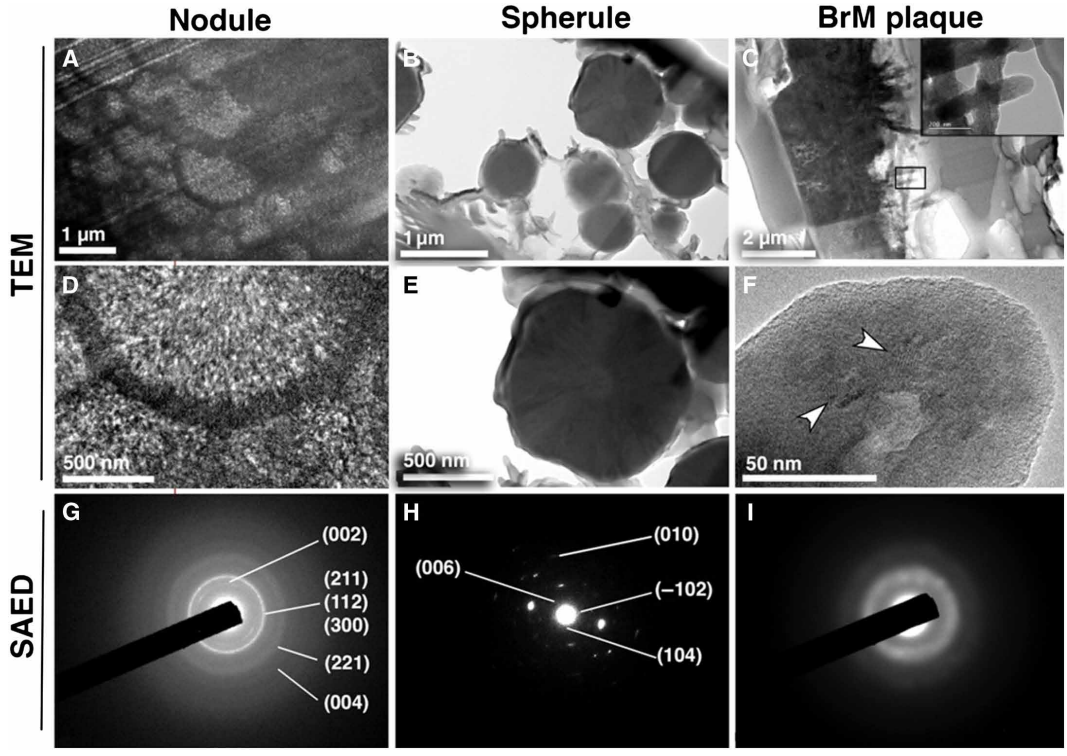

Fig. 5. TEM and SAED of nodules, spherules and plaques. (**A** to **C**) Low-magnification electron micrographs of nodules, spherules, and plaques. (A) Nodules were composed of multiple subunits (lobes) (1 to 20 μm in diameter). (B) Spherules (0.5 to 5 μm in diameter) exhibited increased electron density. (C) Plaques exhibited increased electron density and appeared crossed over and fibrous (inset image). (**D** to **F**) High-magnification electron micrographs of calcific lesions associated with AMD. (D) Single "lobe" subunit of a nodule. Each lobe has an electron-dense crust and a less electron-dense core. (E) Spherules displayed a heterogeneous structure; needle crystal-like structures formed a shell surrounding a less electron-dense core. (F) High-resolution micrograph of a plaque. White arrowheads indicate regions where the lattice is visible. (**G** to **I**) SAED of nodules, spherules, and plaques. A typical diffraction pattern obtained from each lesion is shown. Table S2 details additional reflexions identified by SAED but not indicated on figures. (G) Nodules were indexed to HAP. A sharp diffraction ring for (002) was present, whereas a single diffuse ring was present for reflexions (211), (112), and (300). Rings characteristic of (221) and (004) were also observed. Diffraction patterns for the crust and the core were similar. (H) The mineral component of spherules was identified as whitlockite. Zone axes (010) of whitlockite were identified with vector points for (−102), (006), and (104). (I) Diffraction patterns obtained for BrM plaques produced a diffuse ring characteristic of apatite.

appearance and early studies using the von Kossa stain for phosphates (*34*, *41*–*43*). These highly reflective features are associated with HIRD on OCT and higher rates of incidence of progression to advanced AMD in previous studies from our group, either alone or together with three other indicators (*19*, *21*). OCT-reflective drusen substructures, including ones resembling, stage 4 HIRD (fig. S7) were associated with rapid progression to GA but not to neovascular AMD in a large cohort of patients with intermediate AMD, perhaps because only 14 individuals had this phenotype (*32*). Our study expands this literature by showing in a large patient sample that the hyporeflective cores of drusen confer risk for advancement to both end stages and demonstrating that they are HAP nodules. By appearance and composition, nodules are not simply aggregations of recently described HAP spherules (*10*). Unlike spherules, which are small, refractile on CFP, and reflective on OCT, nodules are large, refractile on CFP, and nonreflective on OCT, a difference that is possibly due to the nodules' rough surface and size. Nodules are hyporeflective like other calcified structures (50 μm to 1 mm) in the posterior eye (*44*, *45*). We suggest that HIRD be called "calcific nodules" going forward instead of alternative terms "hyperreflective pyramidal structures" (*22*) or conical drusen (*32*). Our proposed term describes both the composition and the structure of the hyporeflective core, which our data support as an indicator of AMD progression (*46*). Furthermore, HIRD can now be differentiated from lines with an intense, mirror-like hyperreflectivity in or near BrM that also strongly associate with atrophy (*23*, *24*, *47*–*49*) and may correlate to single or sparse cholesterol crystals (*50*, *51*). These crystals signify replacement of oily drusen with fluid or fibrotic contents that are sufficiently hydrated to support supersaturation and precipitation within this compartment (*50*, *51*).

We observed distinct variations in calcium phosphate phases within specific deposits. Using x-ray diffraction, we previously reported HAP-enriched spherules in drusen (*10*) and in deposits formed by RPE cells in culture (*29*). Combining TEM, EDX spectroscopy, and SAED, we identified highly crystalline whitlockite spherules, polycrystalline HAP nodules, and poorly crystalline apatite plaques. Whitlockite, a magnesium-substituted calcium phosphate previously associated with several diseases (*52*–*54*), is herein reported in human eyes. Preferential whitlockite formation over HAP has been linked to acidic pH and increased magnesium (Mg)–to–calcium (Ca) ratio (*55*, *56*), among other mechanisms. In the kidney, the frequency of apatite and whitlockite phases is unaffected by systemic Mg cation (Mg^{2+}) load (*53*), suggesting that local Mg^{2+} concentration determines which calcium phosphate phase forms. Therefore, appropriate Mg^{2+}

in the sub–RPE-BL space might promote formation of whitlockite spherules (fig. S7). Mg^{2+} can substitute a small proportion of Ca^{2+} in the HAP lattice causing inhibition of HAP crystal growth (*54*, *57*), possibly explaining the restricted size of spherules. In contrast, the absence of Mg^{2+} in nodules may signify that low local Mg^{2+} concentrations facilitate continued crystal growth and thus greater size. Last, despite detectable Mg^{2+} in plaques, the low crystallinity and association of plaque calcification with BrM collagen and elastin (*26*, *58*) did not allow calcium phosphate phases to be identified. After examining numerous sub-RPE deposits of all sizes in our ongoing studies, we are yet to see one without spherules. Thus, we suggest that spherule formation is a natural end point for calcium phosphate formation and Mg^{2+} in the sub–RPE-BL space keeps crystal growth at bay, whereas reduced Mg^{2+} concentrations lead to continuous nodule growth (fig. S7). Our results show that spherules and nodules coexist, but nodules seem to be visible on OCT at the later stages of AMD progression compared to spherules. BrM plaques by their focal spatial confinement can be contrasted with widespread BrM calcification in the inherited disorder pseudoxanthoma elasticum (OMIM 264800) (*59*), suggesting again local pathogenic regulation of mineralization within the druse. In pseudoxanthoma elasticum, BrM is reflective with a rough surface on OCT (*60*); however, whether the smaller plaques in AMD will be similarly visible is not yet known.

What extracellular factors potentially modulate apatite formation in AMD? Organic molecules like functional groups of amino acids, as part of proteins in solution (*61*, *62*), can inhibit HAP formation. However, when immobilized or entrapped on surfaces (*62*, *63*), like in aged BrM, proteins can promote mineral deposition. Similarly, lipids can also nucleate mineral deposition, including both HAP and whitlockite (*64*–*66*). Soft drusen, in which nodules preferentially form, are rich in lipids thought to be derived from RPE-secreted lipoprotein particles in an outer retinal lipid recycling program (*8*, *12*, *13*, *67*, *68*). Direct support for lipid-associated mineralization includes the identification of a cholesterol core within spherules (*10*) and the detection of phosphatidylcholine within sub-RPE deposits produced by confluent and functional RPE cells in culture (*29*). Although the mechanism(s) and full range of contributory proteins and lipids are yet to be identified, our data support a model of organic molecules nucleating inorganic mineral deposits. Once seeded, mineralized surfaces could become sites for further protein deposition (*10*, *29*). Independent of the seeding mechanisms, Ca^{2+} and P supersaturation is essential to initiate mineralization. In tissues, Ca^{2+} availability is tightly regulated with high-affinity binding proteins (*69*), and extracellular phosphate concentration is low (*70*, *71*). Nevertheless, we observed HAP deposition by RPE cells cultured under standard conditions, suggesting that seemingly healthy RPE cells establish an environment conducive to mineral nucleation and growth (*29*). How HAP deposition occurs in vitro and whether whitlockite formation can be promoted by modulating culture medium pH and Mg concentration should now be investigated.

Under "normal" circumstances, neither Mg^{2+} nor Ca^{2+} is available for mineralization in the extracellular space (*72*, *73*). We speculate that with aging, especially pathological aging, this availability changes. In the presence of sufficient extracellular Mg^{2+} and high concentration of Ca^{2+}, spherules may be formed. At low extracellular Mg^{2+} and high Ca^{2+}, the Mg control of mineral growth would be lost so that nodules start proliferating. This proliferation is associated with progression to AMD; therefore, we propose that this condition might associated with increasingly nonfunctional RPE overlying drusen, whereas the presence of functional RPE overlying drusen could help whitlockite spherule formation. A review of data obtained from our RPE culture experiments failed to confirm the presence of Mg^{2+} within the in vitro–mineralized deposits, suggesting that even these apparently functional cells are stressed and in Ca^{2+}-Mg^{2+} imbalance (*29*).

We also considered how extracellular Ca^{2+}-Mg^{2+} imbalance may be influenced by intracellular mechanisms, focusing attention on mitochondria. Mitochondria have stored high concentration of calcium with ultrastructurally visible microparticles of calcium phosphate, and these had been suggested to play a role in extracellular HAP deposition in both healthy (for example, bone) and injured tissues (*74*, *75*). In disease, calcium can be released from the mitochondria through opening of mitochondrial permeability transition pores, leading to swelling, rupture, and release of mitochondrial contents into the cytosol then into the extracellular space (*76*). In eyes with AMD, reduced DICER1 concentration results in accumulation of Alu RNA, which, in turn, is associated with cytosolic release of mitochondrial DNA and presumably Ca^{2+} (*77*). Mitochondrial damage and loss in the human macular RPE is associated with age (*78*), and with AMD severity (*77*, *79*–*81*). Therefore, mitochondrial calcium stores released by failing RPE cells could exit to the extracellular sub–RPE-BL space and tip the Ca^{2+}-Mg^{2+} balance.

Pathways regulating sub-RPE Ca and Mg concentrations are unknown, suggesting aspects of cellular physiology needing exploration. Ca signaling by the RPE is well studied and essential to the activity of apical and basolateral potassium and chloride channels that collectively regulate the ionic environment of photoreceptors, photoreceptor-RPE adherence, and net fluid efflux from retina to choroid (*82*). Ca signaling is also important for health of lysosomes (*83*) needed for RPE processing of ingested photoreceptor tips and diet-delivered lipids. Mg homeostasis is less well studied; although in its ionic form, Mg^{2+} is required by many kinases, including those involved in maintaining apically located, inward-rectifying potassium currents in RPE (*84*, *85*). Furthermore, developmental Mg deficiency causes focal RPE degeneration and excess Ca/Mg ratio in retina (*86*).

Strengths of this study include multidisciplinary converging evidence showing three distinct refractile structures associated with GA: (i) small highly crystalline whitlockite spherules that account for hyperreflective dots on OCT and NIR, (ii) large nodules containing polycrystalline calcium phosphate and appearing hyporeflective on OCT and isoreflective on NIR, and (iii) amorphous crystalline plaques in BrM. Common features among these are Ca- and P-containing mineralization signifying molecular processes that can now be informed by research relevant to other conditions. Limitations include the small number of samples available for mineralomic characterization and the current lack of an imaging correlate for BrM plaques. Future directions include extending the clinical observations to other patient cohorts, identification of imaging signatures before calcification, and exploring whether local and systemic Ca^{2+} and Mg^{2+} regulation are targets for AMD treatment and prevention, because current clinical data are mixed (*87*–*89*). We conclude that extracellular mineralization in the form of nodules indicates risk for progression to late AMD because it reveals the agonal state of the overlying RPE. Elucidating the timeline of RPE demise by imaging mineralization may help direct new therapeutic approaches to disease stages earlier than GA.

MATERIALS AND METHODS

Study design

Both clinical cohorts were approved by their respective institutional review boards and complied with the Health Insurance Portability and Accountability Act of 1996 and the Declaration of Helsinki. The use of human tissue samples was approved by the institutional review boards at the University of Alabama at Birmingham and University College London.

Cohort 1 of patients with AMD for multimodal imaging of defined deposits

To establish stages of deposit progression, a cohort of consecutive patients with HIRD on OCT imaging, seen by a single retinal specialist (K.B.F.) at a tertiary private retinal practice, was retrospectively reviewed. Inclusion criteria were eyes with GA with at least one HIRD seen on OCT and with at least a 3-year follow-up with OCT volume scans taken on at least 10 consecutive visits. The exclusion criteria included the presence of any neovascular AMD during the course of follow-up, other retinal vascular or degenerative diseases, and eyes with significant media opacity that affected imaging quality.

Cohort 2 of eyes with intermediate AMD for longitudinal observation

To establish the prevalence and progression risk of HIRD, a cohort with a total of 840 eyes of 420 consecutive patients with AMD seen by a single retinal specialist (S.R.S.) between 2010 and 2014 in a tertiary care academic retinal practice in Los Angeles was retrospectively reviewed. From this dataset, we selected all subjects who had at least one eye with evidence of intermediate AMD, defined according to the Beckman classification (*90*), no other posterior segment ocular disease, dense OCT volume scans (Cirrus OCT with 128 B-scans over a 6-mm by 6-mm region centered on the fovea), and at least 12 months of follow-up data including OCT. Dense-volume scans with spacing less than 50 μm between scans were required to avoid missing the center of large drusenoid lesions between B-scans. Finding the center was critical for reliable assessment of druse core reflectivity characteristics. Twelve months of follow-up data were required. When both eyes of one subject met these inclusion criteria, one eye was randomly selected for analysis. A total of 138 eyes from 138 subjects met these criteria. OCT scans at baseline were reviewed by certified OCT graders at the Doheny Image Reading Center to assess for presence of hyporeflective cores within the drusen. Graders were masked as to other clinical data regarding the patients. Clinical charts and follow-up imaging data were evaluated over the next 12 months to ascertain the frequency of progression GA or CNV.

Imaging-histology correlations in donor eyes with AMD

Spectral domain OCT imaging of human donor eyes followed by high-resolution histology provided a link between clinical imaging and microanalysis of selected drusen. Three separate series of eyes were reviewed for suitable specimens, all drawn from a repository of ≥900 pairs of donor eyes accessioned from the Alabama Eye Bank for research purposes (1995–2012). (i) Eyes for OCT imaging and histology (Figs. 2 and 3) were used for the creation of the Project MACULA online AMD histology resource (http://projectmacula.cis.uab.edu/) (139 maculas), and median death-to-preservation time was 3.62 hours (range, 0.67 to 12.15 hours). These were subject to ex vivo multimodal imaging including OCT, NIR, and 488- and 787-nm FAF using a custom tissue holder and a Spectralis HRA+OCT (Heidelberg Engineering), in addition to digital color photography (*50*). Specimens were post-fixed in osmium tannic acid paraphenylenediamine to preserve extracellular lipid, embedded in epoxy resin, sectioned at 0.8 μm, and stained with toluidine blue (*34*). (ii) For advanced mineralomics, one eye with distinctive glistening drusen from the ALARMGS series of eyes (n = 30) (*34*) was used and shown in fig. S2. All eyes underwent ex vivo color photography using epi- and trans-scleral illumination, followed by post-fixation in osmium only, en bloc staining with uranyl acetate, and epoxy embedding. (iii) For advanced mineralomics in Figs. 4 and 5, four blocks of four eyes were taken from a series of nine eyes of seven donors with large macular drusen imaged by ex vivo color photography, microdissected, post-fixed by the osmium tannic acid paraphenylenediamine method, and histologically confirmed as having spherules and/or nodules (*35*).

In addition to these clinically undocumented eyes, one eye of a patient with in vivo clinical OCT was used for direct clinicopathologic correlation (Fig. 2, A to D). An 86-year-old white woman had GA in the left eye. Four months after her last clinic visit and 7.5 hours after death, eyes were recovered and preserved as described (*91*). Histology proceeded as described above for series 1.

Sample source for mineralomic studies

Human cadaveric eyes with sub-RPE deposits and BrM plaques were obtained from the University College London Institute of Ophthalmology and Moorfield's Eye Hospital Tissue Repository. Cadaveric eyes were enucleated 12 to 24 hours after death and preserved in 1% glutaraldehyde with 4% paraformaldehyde. Spherules, nodules, and plaques were identified in these specimens by comparison of morphology to specimens with clinical and/or ex vivo imaging documentation of AMD with large macular drusen, as described above.

Statistical analysis

For cohort 1, statistical analysis was performed using an online statistical calculator (http://vassarstats.net/), and $P < 0.05$ was considered significant. To determine whether there was a significant difference in appearance of the two variant stages, the Fisher's exact test was used (fig. S8 and dataset S1). For cohort 2, binary logistic regression was performed to determine the influence of HIRD on the progression to either GA or CNV using SPSS Statistics for Windows (released 2016, version 24.0.). Because of the lack of multiples of clinically highly characterized samples, statistical analysis was not applied to the mineralomic studies, but representative samples were used and presented throughout (see table S2).

SUPPLEMENTARY MATERIALS

www.sciencetranslationalmedicine.org/cgi/content/full/10/466/eaat4544/DC1

Fig. S1. Appearance of HIRD as seen on multimodal imaging during progression.
Fig. S2. Refractile drusen with nodules and RPE atrophy in the index case for microanalysis.
Fig. S3. SEM of isolated nodules.
Fig. S4. Density-dependent SEM of calcific lesions.
Fig. S5. Synchrotron microfocus x-ray fluorescence confirms the presence of Ca in large nodules.
Fig. S6. TOF-SIMS confirms the presence of HAP within nodules.
Fig. S7. Proposed progression stages of calcified structures in AMD.
Fig. S8. Two variants of HIRD.
Table S1. Composition and appearance of calcified structures in eyes with GA as revealed by multimodal clinical and molecular imaging.
Table S2. Table of sample sources.

Table S3. D-spacings and I/I_{max} (%) of candidate calcium phosphate compounds.
Dataset S1. Primary data from cohort 1.
Dataset S2. Primary data from cohort 2.
Movie S1. Progression of nodules, spherules, and BrM plaques.

REFERENCES AND NOTES

1. W. L. Wong, X. Su, X. Li, C. M. Cheung, R. Klein, C. Y. Cheng, T. Y. Wong, Global prevalence of age-related macular degeneration and disease burden projection for 2020 and 2040: A systematic review and meta-analysis. *Lancet Glob. Health* **2**, e106–e116 (2014).
2. Comparison of Age-related Macular Degeneration Treatments Trials (CATT) Research Group, M. G. Maguire, D. F. Martin, G. S. Ying, G. J. Jaffe, E. Daniel, J. E. Grunwald, C. A. Toth, F. L. Ferris III, S. L. Fine, Five-year outcomes with anti–vascular endothelial growth factor treatment of neovascular age-related macular degeneration: The Comparison of age-related macular degeneration treatments trials. *Ophthalmology* **123**, 1751–1761 (2016).
3. U. Chakravarthy, C. C. Bailey, R. L. Johnston, M. McKibbin, R. S. Khan, S. Mahmood, L. Downey, N. Dhingra, C. Brand, C. J. Brittain, J. R. Willis, S. Rabhi, A. Muthutantri, R. A. Cantrell, Characterizing disease burden and progression of geographic atrophy secondary to age-related macular degeneration. *Ophthalmology* **125**, 842–849 (2018).
4. T. G. Farkas, V. Sylvester, D. Archer, M. Altona, The histochemistry of drusen. *Am. J. Ophthalmol.* **71**, 1206–1215 (1971).
5. D. Pauleikhoff, S. Zuels, G. S. Sheraidah, J. Marshall, A. Wessing, A. C. Bird, Correlation between biochemical composition and fluorescein binding of deposits in Bruch's membrane. *Ophthalmology* **99**, 1548–1553 (1992).
6. C. A. Curcio, C. L. Millican, T. Bailey, H. S. Kruth, Accumulation of cholesterol with age in human Bruch's membrane. *Invest. Ophthalmol. Vis. Sci.* **42**, 265–274 (2001).
7. R. Haimovici, D. L. Gantz, S. Rumelt, T. F. Freddo, D. M. Small, The lipid composition of drusen, Bruch's membrane, and sclera by hot stage polarizing light microscopy. *Invest. Ophthalmol. Vis. Sci.* **42**, 1592–1599 (2001).
8. C. A. Curcio, J. B. Presley, G. Malek, N. E. Medeiros, D. V. Avery, H. S. Kruth, Esterified and unesterified cholesterol in drusen and basal deposits of eyes with age-related maculopathy. *Exp. Eye Res.* **81**, 731–741 (2005).
9. J. M. Flinn, P. Kakalec, R. Tappero, B. Jones, I. Lengyel, Correlations in distribution and concentration of calcium, copper and iron with zinc in isolated extracellular deposits associated with age-related macular degeneration. *Metallomics* **6**, 1223–1228 (2014).
10. R. B. Thompson, V. Reffatto, J. G. Bundy, E. Kortvely, J. M. Flinn, A. Lanzirotti, E. A. Jones, D. S. McPhail, S. Fearn, K. Boldt, M. Ueffing, S. G. Ratu, L. Pauleikhoff, A. C. Bird, I. Lengyel, Identification of hydroxyapatite spherules provides new insight into subretinal pigment epithelial deposit formation in the aging eye. *Proc. Natl. Acad. Sci. U.S.A.* **112**, 1565–1570 (2015).
11. J. W. Crabb, M. Miyagi, X. Gu, K. Shadrach, K. A. West, H. Sakaguchi, M. Kamei, A. Hasan, L. Yan, M. E. Rayborn, R. G. Salomon, J. G. Hollyfield, Drusen proteome analysis: An approach to the etiology of age-related macular degeneration. *Proc. Natl. Acad. Sci. U.S.A.* **99**, 14682–14687. (2002).
12. G. Malek, C.-M. Li, C. Guidry, N. E. Medeiros, C. A. Curcio, Apolipoprotein B in cholesterol-containing drusen and basal deposits of human eyes with age-related maculopathy. *Am. J. Pathol.* **162**, 413–425 (2003).
13. L. Wang, M. E. Clark, D. K. Crossman, K. Kojima, J. D. Messinger, J. A. Mobley, C. A. Curcio, Abundant lipid and protein components of drusen. *PLOS ONE* **5**, e10329 (2010).
14. A. L. Fett, M. M. Hermann, P. S. Muether, B. Kirchhof, S. Fauser, Immunohistochemical localization of complement regulatory proteins in the human retina. *Histol. Histopathol.* **27**, 357–364 (2012).
15. J. P. Sarks, S. H. Sarks, M. C. Killingsworth, Evolution of soft drusen in age-related macular degeneration. *Eye* **8**, 269–283 (1994).
16. C. A. Curcio, Soft drusen in age-related macular degeneration: Biology and targeting, via the oil spill strategy. *Invest. Ophthalmol. Vis. Sci.* **59**, AMD160–AMD181 (2018).
17. F. G. Holz, S. Sadda, G. Staurenghi, M. Lindner, A. C. Bird, B. A. Blodi, B. Bottoni, U. Chakravarthy, E. Chew, K. Csaky, C. A. Curcio, R. Danis, K. B. Freund, J. Grunwald, R. Guymer, C. Hoyng, G. J. Jaffe, S. Liakopoulos, J. Monés, A. Oishi, D. Pauleikhoff, P. J. Rosenfeld, D. Sarraf, R. F. Spaide, R. Tadayoni, A. Tufail, S. Wolf, S. Schmitz-Valckenberg; CAM Group, Imaging protocols for clinical studies in age-related macular degeneration. Recommendations from Classification of Atrophy (CAM) Consensus Meeting. *Ophthalmology* **124**, 464–478 (2017).
18. S. T. Garrity, D. Sarraf, K. B. Freund, S. R. Sadda, Multimodal imaging of nonneovascular age-related macular degeneration. *Invest. Ophthalmol. Vis. Sci.* **59**, AMD48–AMD64 (2018).
19. J. Lei, S. Balasubramanian, N. S. Abdelfattah, M. Nittala, S. R. Sadda, Proposal of a simple optical coherence tomography-based scoring system for progression of age related macular degeneration. *Graefes Arch. Clin. Exp. Ophthalmol.* **255**, 1551–1558 (2017).
20. M. Suzuki, C. A. Curcio, R. F. Mullins, R. F. Spaide, Refractile drusen: Clinical imaging and candidate histology. *Retina* **35**, 859–865 (2015).
21. Y. Ouyang, F. M. Heussen, A. Hariri, P. A. Keane, S. R. Sadda, Optical coherence tomography-based observation of the natural history of drusenoid lesion in eyes with dry age-related macular degeneration. *Ophthalmology* **120**, 2656–2665 (2013).
22. C. Bonnet, G. Querques, J. Zerbib, H. Oubraham, R. B. Garavito, N. Puche, E. H. Souied, Hyperreflective pyramidal structures on optical coherence tomography in geographic atrophy areas. *Retina* **34**, 1524–1530 (2014).
23. M. Fleckenstein, P. Charbel Issa, H. M. Helb, S. Schmitz-Valckenberg, R. P. Finger, H. P. Scholl, K. U. Loeffler, F. G. Holz, High-resolution spectral domain-OCT imaging in geographic atrophy associated with age-related macular degeneration. *Invest. Ophthalmol. Vis. Sci.* **49**, 4137–4144 (2008).
24. K. Moussa, J. Y. Lee, S. S. Stinnett, G. J. Jaffe, Spectral domain optical coherence tomography-determined morphologic predictors of age-related macular degeneration-associated geographic atrophy progression. *Retina* **33**, 1590–1599 (2013).
25. R. J. Ulshafer, C. B. Allen, B. Nicolaissen Jr., M. L. Rubin, Scanning electron microscopy of human drusen. *Invest. Ophthalmol. Vis. Sci.* **28**, 683–689. (1987).
26. T. L. van der Schaft, W. C. de Bruijn, C. M. Mooy, D. A. M. Ketelaars, P. T. V. M. de Jong, Element analysis of the early stages of age-related macular degeneration. *Arch. Ophthalmol.* **110**, 389–394 (1992).
27. S. D. Vogt, C. A. Curcio, L. Wang, C.-M. Li, G. McGwin Jr., N. E. Medeiros, N. J. Philp, J. A. Kimble, R. W. Read, Retinal pigment epithelial expression of complement regulator CD46 is altered early in the course of geographic atrophy. *Exp. Eye Res.* **93**, 413–423 (2011).
28. W. L. Davis, R. G. Jones, H. K. Hagler, An electron microscopic histochemical and analytical X-ray microprobe study of calcification in Bruch's membrane from human eyes. *J. Histochem. Cytochem.* **29**, 601–608. (1981).
29. M. G. Pilgrim, I. Lengyel, A. Lanzirotti, M. Newville, S. Fearn, E. Emri, J. C. Knowles, J. D. Messinger, R. W. Read, C. Guidry, C. A. Curcio, Subretinal pigment epithelial deposition of drusen components including hydroxyapatite in a primary cell culture model. *Invest. Ophthalmol. Vis. Sci.* **58**, 708–719 (2017).
30. P. Fratzl, R. Weinkamer, Nature's hierarchical materials. *Prog. Mater. Sci.* **52**, 1263–1334 (2007).
31. S. Bertazzo, E. Gentleman, K. L. Cloyd, A. H. Chester, M. H. Yacoub, M. M. Stevens, Nano-analytical electron microscopy reveals fundamental insights into human cardiovascular tissue calcification. *Nat. Mater.* **12**, 576–583 (2013).
32. M. Veerappan, A. M. El-Hage-Sleiman, V. Tai, S. J. Chiu, K. P. Winter, S. S. Stinnett, T. S. Hwang, G. B. Hubbard III, M. Michelson, R. Gunther, W. T. Wong, E. Y. Chew, C. A. Toth; Age-related Eye Disease Study 2 Ancillary Spectral Domain Optical Coherence Tomography Study Group, Optical coherence tomography reflective drusen substructures predict progression to geographic atrophy in age-related macular degeneration. *Ophthalmology* **123**, 2554–2570 (2016).
33. J. P. Sarks, S. H. Sarks, M. C. Killingsworth, Evolution of geographic atrophy of the retinal pigment epithelium. *Eye* **2**, 552–577 (1988).
34. C. A. Curcio, N. E. Medeiros, C. L. Millican, The Alabama age-related macular degeneration grading system for donor eyes. *Invest. Ophthalmol. Vis. Sci.* **39**, 1085–1096 (1998).
35. M. Rudolf, M. E. Clark, M. Chimento, C.-M. Li, N. E. Medeiros, C. A. Curcio, Prevalence and morphology of druse types in the macula and periphery of eyes with age-related maculopathy. *Invest. Ophthalmol. Vis. Sci.* **49**, 1200–1209 (2008).
36. P. Malmberg, H. Nygren, Methods for the analysis of the composition of bone tissue, with a focus on imaging mass spectrometry (TOF-SIMS). *Proteomics* **8**, 3755–3762 (2008).
37. B. D. Cullity, S. R. Stock, *Elements of X-Ray Diffraction* (Pearson, 2001).
38. P. J. Rosenfeld, Optical coherence tomography and the development of antiangiogenic therapies in neovascular age-related macular degeneration. *Invest. Ophthalmol. Vis. Sci.* **57**, OCT14–OCT26 (2016).
39. C. Balaratnasingam, J. D. Messinger, K. R. Sloan, L. A. Yannuzzi, K. B. Freund, C. A. Curcio, Histologic and optical coherence tomographic correlations in drusenoid pigment epithelium detachment in age-related macular degeneration. *Ophthalmology* **124**, 644–656 (2017).
40. C. A. Curcio, E. C. Zanzottera, T. Ach, C. Balaratnasingam, K. B. Freund, Activated retinal pigment epithelium, an optical coherence tomography biomarker for progression in age-related macular degeneration. *Invest. Ophthalmol. Vis. Sci.* **58**, BIO211–BIO226 (2017).
41. J. D. M. Gass, Pathogenesis of disciform detachment of the neuroepithelium. III. Senile disciform macular degeneration. *Am. J. Ophthalmol.* **63**, 617–644 (1967).
42. W. R. Green, S. N. Key III, Senile macular degeneration: A histopathologic study. *Trans. Am. Ophthalmol. Soc.* **75**, 180–254 (1977).
43. N. M. Bressler, J. C. Silva, S. B. Bressler, S. L. Fine, W. R. Green, Clinicopathological correlation of drusen and retinal pigment epithelial abnormalities in age-related macular degeneration. *Retina* **14**, 130–142 (1994).
44. F. Pichi, D. Massaro, M. Serafino, P. Carrai, G. P. Giuliari, C. L. Shields, C. Veronese, A. P. Ciardella, P. Nucci, Retinal astrocytic hamartoma: Optical coherence tomography classification and correlation with tuberous sclerosis complex. *Retina* **36**, 1199–1208 (2016).
45. T. Sato, S. Mrejen, R. F. Spaide, Multimodal imaging of optic disc drusen. *Am. J. Ophthalmol.* **156**, 275–282.e1 (2013).

46. Y. Ouyang, F. M. Heussen, P. A. Keane, R. K. R. Pappuru, S. R. Sadda, A. C. Walsh, Juxtapapillary pigment epithelium detachment observed in asymptomatic participants using optical coherence tomography. *Invest. Ophthalmol. Vis. Sci.* **54**, 1144–1149 (2013).
47. G. Querques, A. Georges, N. Ben Moussa, M. Sterkers, E. H. Souied, Appearance of regressing drusen on optical coherence tomography in age-related macular degeneration. *Ophthalmology* **121**, 173–179 (2014).
48. M. J. Heiferman, A. A. Fawzi, Discordance between blue-light autofluorescence and near-infrared autofluorescence in age-related macular degeneration. *Retina* **36** (suppl. 1), S137–S146 (2016).
49. A. Oishi, S. Thiele, J. Nadal, M. Oishi, M. Fleckenstein, M. Schmid, F. G. Holz, S. Schmitz-Valckenberg, Prevalence, natural course, and prognostic role of refractile drusen in age-related macular degeneration. *Invest. Ophthalmol. Vis. Sci.* **58**, 2198–2206 (2017).
50. C. Pang, J. D. Messinger, E. C. Zanzottera, K. B. Freund, C. A. Curcio, The Onion Sign in neovascular age-related macular degeneration represents cholesterol crystals. *Ophthalmology* **122**, 2316–2326 (2015).
51. M. Li, R. Dolz-Marco, J. D. Messinger, K. R. Sloan, D. Ferrara, C. A. Curcio, K. B. Freund, Clinicopathologic correlation of aneurysmal type 1 neovascularization in age-related macular degeneration. *Ophthalmol. Retina* (2018).
52. S. C. Verberckmoes, V. Persy, G. J. Behets, E. Neven, A. Hufkens, H. Zebger-Gong, D. Muller, D. Haffner, U. Querfeld, S. Bohic, M. E. De Broe, P. C. D'Haese, Uremia-related vascular calcification: More than apatite deposition. *Kidney Int.* **71**, 298–303 (2007).
53. D.-C. Fischer, G. J. Behets, O. W. Hakenberg, M. Voigt, B. A. Vervaet, S. Robijn, G. Kundt, W. Schareck, P. C. D'Haese, D. Haffner, Arterial microcalcification in atherosclerotic patients with and without chronic kidney disease: A comparative high-resolution scanning X-ray diffraction analysis. *Calcif. Tissue Int.* **90**, 465–472 (2012).
54. R. Lagier, C. A. Baud, Magnesium whitlockite, a calcium phosphate crystal of special interest in pathology. *Pathol. Res. Pract.* **199**, 329–335 (2003).
55. T. Kani, M. Kani, Y. Moriwaki, Y. Doi, Microbeam x-ray diffraction analysis of dental calculus. *J. Dent. Res.* **62**, 92–95 (1983).
56. A. C. Tas, Synthesis of biomimetic Ca-hydroxyapatite powders at 37°C in synthetic body fluids. *Biomaterials* **21**, 1429–1438 (2000).
57. R. Villa-Bellosta, Impact of magnesium:calcium ratio on calcification of the aortic wall. *PLOS ONE* **12**, e0178872 (2017).
58. M. J. Hogan, J. A. Alvarado, J. E. Weddell, *Histology of the Human Eye. An Atlas and Textbook* (W. B. Saunders, 1971), pp. 328–363.
59. O. A. Jensen, Bruch's membrane in pseudoxanthoma elasticum. Histochemical, ultrastructural, and x-ray microanalytical study of the membrane and angioid streak areas. *Albrecht Von Graefes Arch. Klin. Exp. Ophthalmol.* **203**, 311–320 (1977).
60. M. Gliem, R. Fimmers, P. L. Muller, C. K. Brinkmann, R. P. Finger, D. Hendig, F. G. Holz, P. C. Issa, Choroidal changes associated with Bruch membrane pathology in pseudoxanthoma elasticum. *Am. J. Ophthalmol.* 158, 644 (2014).
61. I. Hirata, M. Akamatsu, E. Fujii, S. Poolthong, M. Okazaki, Chemical analyses of hydroxyapatite formation on SAM surfaces modified with COOH, NH_2, CH_3, and OH functions. *Dent. Mater. J.* **29**, 438–445 (2010).
62. G. H. Nancollas, M. LoRe, L. Perez, C. Richardson, S. J. Zawacki, Mineral phases of calcium phosphate. *Anat. Rec.* **224**, 234–241 (1989).
63. A. Linde, A. Lussi, M. A. Crenshaw, Mineral induction by immobilized polyanionic proteins. *Calcif. Tissue Int.* **44**, 286–295 (1989).
64. C. L. Raggio, B. D. Boyan, A. L. Boskey, In vivo hydroxyapatite formation induced by lipids. *J. Bone Miner. Res.* **1**, 409–415 (1986).
65. C. A. Scotchford, S. Y. Ali, Magnesium whitlockite deposition in articular cartilage: A study of 80 specimens from 70 patients. *Ann. Rheum. Dis.* **54**, 339–344 (1995).
66. C. A. Scotchford, S. Y. Ali, Association of magnesium whitlockite crystals with lipid components of the extracellular matrix in human articular cartilage. *Osteoarthritis Cartilage* **5**, 107–119 (1997).
67. C. A. Curcio, M. Johnson, M. Rudolf, J.-D. Huang, The oil spill in ageing Bruch membrane. *Br. J. Ophthalmol.* **95**, 1638–1645 (2011).
68. C. A. Curcio, Antecedents of soft drusen, the specific deposit of age-related macular degeneration, in the biology of human macula. *Invest. Ophthalmol. Vis. Sci.* **59**, AMD182–AMD194 (2018).
69. W. Jahnen-Dechent, A. Heiss, C. Schäfer, M. Ketteler, Fetuin-A regulation of calcified matrix metabolism. *Circ. Res.* **108**, 1494–1509 (2011).
70. W. L. Lau, M. H. Festing, C. M. Giachelli, Phosphate and vascular calcification: Emerging role of the sodium-dependent phosphate co-transporter PiT-1. *Thromb. Haemost.* **104**, 464–470 (2010).
71. E. Lederer, Regulation of serum phosphate. *J. Physiol.* **592**, 3985–3995 (2014).
72. W. Jahnen-Dechent, M. Ketteler, Magnesium basics. *Clin. Kidney J.* **5**, i3–i14 (2012).
73. A. M. Hofer, E. M. Brown, Extracellular calcium sensing and signalling. *Nat. Rev. Mol. Cell Biol.* **4**, 530–538 (2003).
74. A. L. Lehninger, Mitochondria and calcium ion transport. *Biochem. J.* **119**, 129–138 (1970).
75. S. Boonrungsiman, E. Gentleman, R. Carzaniga, N. D. Evans, D. W. McComb, A. E. Porter, M. M. Stevens, The role of intracellular calcium phosphate in osteoblast-mediated bone apatite formation. *Proc. Natl. Acad. Sci. U.S.A.* **109**, 14170–14175 (2012).
76. L. Galluzzi, K. Blomgren, G. Kroemer, Mitochondrial membrane permeabilization in neuronal injury. *Nat. Rev. Neurosci.* **10**, 481–494 (2009).
77. H. Kaneko, S. Dridi, V. Tarallo, B. D. Gelfand, B. J. Fowler, W. G. Cho, M. E. Kleinman, S. L. Ponicsan, W. W. Hauswirth, V. A. Chiodo, K. Kariko, J. W. Yoo, D. K. Lee, M. Hadziahmetovic, Y. Song, S. Misra, G. Chaudhuri, F. W. Buaas, R. E. Braun, D. R. Hinton, Q. Zhang, H. E. Grossniklaus, J. M. Provis, M. C. Madigan, A. H. Milam, N. L. Justice, R. J. Albuquerque, A. D. Blandford, S. Bogdanovich, Y. Hirano, J. Witta, E. Fuchs, D. R. Littman, B. K. Ambati, C. M. Rudin, M. M. Chong, P. Provost, J. F. Kugel, J. A. Goodrich, J. L. Dunaief, J. Z. Baffi, J. Ambati, DICER1 deficit induces *Alu* RNA toxicity in age-related macular degeneration. *Nature* **471**, 325–330 (2011).
78. J. Feher, I. Kovacs, M. Artico, C. Cavallotti, A. Papale, C. Balacco Gabrieli, Mitochondrial alterations of retinal pigment epithelium in age-related macular degeneration. *Neurobiol. Aging* **27**, 983–993 (2006).
79. M. R. Terluk, R. J. Kapphahn, L. M. Soukup, H. Gong, C. Gallardo, S. R. Montezuma, D. A. Ferrington, Investigating mitochondria as a target for treating age-related macular degeneration. *J. Neurosci.* **35**, 7304–7311 (2015).
80. C. L. Nordgaard, P. P. Karunadharma, X. Feng, T. W. Olsen, D. A. Ferrington, Mitochondrial proteomics of the retinal pigment epithelium at progressive stages of age-related macular degeneration. *Invest. Ophthalmol. Vis. Sci.* **49**, 2848–2855 (2008).
81. N. Kerur, S. Fukuda, D. Banerjee, Y. Kim, D. Fu, I. Apicella, A. Varshney, R. Yasuma, B. J. Fowler, E. Baghdasaryan, K. M. Marion, X. Huang, T. Yasuma, Y. Hirano, V. Serbulea, M. Ambati, V. L. Ambati, Y. Kajiwara, K. Ambati, S. Hirahara, A. Bastos-Carvalho, Y. Ogura, H. Terasaki, T. Oshika, K. B. Kim, D. R. Hinton, N. Leitinger, J. C. Cambier, J. D. Buxbaum, M. C. Kenney, S. M. Jazwinski, H. Nagai, I. Hara, A. P. West, K. A. Fitzgerald, S. R. Sadda, B. D. Gelfand, J. Ambati, cGAS drives noncanonical-inflammasome activation in age-related macular degeneration. *Nat. Med.* **24**, 50–61 (2018).
82. K. J. Miyagishima, Q. Wan, B. Corneo, R. Sharma, M. R. Lotfi, N. C. Boles, F. Hua, A. Maminishkis, C. Zhang, T. Blenkinsop, V. Khristov, B. S. Jha, O. S. Memon, S. D'Souza, S. Temple, S. S. Miller, K. Bharti, In pursuit of authenticity: Induced pluripotent stem cell-derived retinal pigment epithelium for clinical applications. *Stem Cells Transl. Med.* **5**, 1562–1574 (2016).
83. N. M. Gómez, W. Lu, J. C. Lim, K. Kiselyov, K. E. Campagno, Y. Grishchuk, S. A. Slaugenhaupt, B. A. Pfeffer, S. J. Fliesler, C. H. Mitchell, Robust lysosomal calcium signaling through channel TRPML1 is impaired by lysosomal lipid accumulation. *FASEB J.* **32**, 782–794 (2017).
84. B. R. Pattnaik, B. A. Hughes, Regulation of Kir channels in bovine retinal pigment epithelial cells by phosphatidylinositol 4,5-bisphosphate. *Am. J. Physiol. Cell Physiol.* **297**, C1001–C1011 (2009).
85. X. Zhang, B. A. Hughes, KCNQ and KCNE potassium channel subunit expression in bovine retinal pigment epithelium. *Exp. Eye Res.* **116**, 424–432 (2013).
86. H. Gong, T. Amemiya, K. Takaya, Retinal changes in magnesium-deficient rats. *Exp. Eye Res.* **72**, 23–32 (2001).
87. C. L. M. Kakigi, K. Singh, S. Y. Wang, W. T. Enanoria, S. C. Lin, Self-reported calcium supplementation and age-related macular degeneration. *JAMA Ophthalmol.* **133**, 746–754 (2015).
88. B. Gopinath, V. M. Flood, J. C. Y. Louie, J. J. Wang, G. Burlutsky, E. Rochtchina, P. Mitchell, Consumption of dairy products and the 15-year incidence of age-related macular degeneration. *Br. J. Nutr.* **111**, 1673–1679 (2014).
89. R. Klein, B. E. Klein, S. C. Jensen, K. J. Cruickshanks, K. E. Lee, L. G. Danforth, S. C. Tomany, Medication use and the 5-year incidence of early age-related maculopathy: The Beaver Dam Eye Study. *Arch. Ophthalmol.* **119**, 1354–1359. (2001).
90. F. L. Ferris III, C. P. Wilkinson, A. Bird, U. Chakravarthy, E. Chew, K. Csaky, S. R. Sadda; Beckman Initiative for Macular Research Classification Committee, Clinical classification of age-related macular degeneration. *Ophthalmology* **120**, 844–851 (2013).
91. M. Li, R. Dolz-Marco, J. D. Messinger, L. Wang, R. M. Feist, C. A. Girkin, S. Gattoussi, D. Ferrara, C. A. Curcio, K. B. Freund, Clinicopathologic correlation of anti-vascular endothelial growth factor-treated type 3 neovascularization in age-related macular degeneration. *Ophthalmology* **125**, 276–287 (2018).

Acknowledgments: We thank R. A. Martin, O. Addison, A. C. Bird, and J. Knowles for their help and advice. Human donor eyes in Figs. 2 and 3 were recovered by the Alabama Eye Bank. Some of the tissues for this project were provided by the University College London Institute of Ophthalmology and Moorfields Eye Hospital Eye Tissue Repository. **Funding:** The research was supported by the Bill Brown Charitable Trust Senior Research Fellowship, Moorfields Eye Hospital Special Trustees, and the European Union's Horizon 2020 research and innovation program under grant agreement no. 634479 for the "Eye-Risk" project (to I.L.). The tissue repository was supported by funding from the National Institute for Health Research.

The Project MACULA website and the recovery of human donor eyes for research were supported by the National Institutes of Health (grant nos. R01EY06019 and P30EY003039), the EyeSight Foundation of Alabama, the International Retinal Research Foundation, the Edward N. and Della L. Thome Foundation, the Arnold and Mabel Beckman Initiative for Macular Research, and Research to Prevent Blindness Inc. (New York, NY). Diamond Light Source (Harwell Science and Innovation Campus, Didcot, Oxfordshire OX11 0DE, UK) provided access to Beamline I18. The TOF-SIMS analysis was supported by the Engineering and Physical Sciences Research Council, UK (grant EP/H006060/1) and by the Natural Environment Research Council, UK (grant NE/J013382/1). **Author contributions:** Multimodal imaging and analysis of cohort 1: A.C.S.T.; mineralomics: M.G.P., I.L., S.F., S.B., E.T., and A.P.M.; imaging-histology correlations: M.L., J.D.M., and C.A.C.; patients and analysis for cohort 2: J.L., M.G.N., and S.R.S.; patients for cohort 1: R.D.-M. and K.B.F.; drafting of the manuscript: A.C.S.T., M.G.P., I.L., S.R.S., and C.A.C.; revision of manuscript, all authors; scientific direction, I.L., K.B.F., and C.A.C. **Competing interests:** M.L. received research support from Hoffman LaRoche. K.B.F. is a consultant to Genentech, Bayer HealthCare, Optovue, ThromboGenics, Ohr Pharmaceutical, and Heidelberg Engineering (honorarium for each). R.D.-M. receives research support from Alcon, Genentech, Heidelberg Engineering, Novartis, and Roche. C.A.C. received research support from Hoffman LaRoche and Heidelberg Engineering. S.R.S. is a consultant for Optos, Carl Zeiss Meditec, Centervue, Heidelberg Engineering, Allergan, Roche, Novartis, Iconic, and Thrombogenics and received research support from Optos, Carl Zeiss Meditec, Allergan, and Genentech. I.L. receives unrestricted research support from Optos. All other authors declare that they have no competing interests. **Data and materials availability:** All data are present in the main manuscript or in the Supplementary Materials.

Submitted 9 March 2018
Resubmitted 10 August 2018
Accepted 17 October 2018
Published 7 November 2018
10.1126/scitranslmed.aat4544

Citation: A. C. S. Tan, M. G. Pilgrim, S. Fearn, S. Bertazzo, E. Tsolaki, A. P. Morrell, M. Li, J. D. Messinger, R. Dolz-Marco, J. Lei, M. G. Nittala, S. R. Sadda, I. Lengyel, K. B. Freund, C. A. Curcio, Calcified nodules in retinal drusen are associated with disease progression in age-related macular degeneration. *Sci. Transl. Med.* **10**, eaat4544 (2018).

Science Translational Medicine

Calcified nodules in retinal drusen are associated with disease progression in age-related macular degeneration

Anna C. S. Tan, Matthew G. Pilgrim, Sarah Fearn, Sergio Bertazzo, Elena Tsolaki, Alexander P. Morrell, Miaoling Li, Jeffrey D. Messinger, Rosa Dolz-Marco, Jianqin Lei, Muneeswar G. Nittala, Srinivas R. Sadda, Imre Lengyel, K. Bailey Freund and Christine A. Curcio

Sci Transl Med **10**, eaat4544.
DOI: 10.1126/scitranslmed.aat4544

Imaging AMD progression

Age-related macular degeneration (AMD) is the leading cause of vision impairment in older individuals. About 20% of those who develop AMD will progress to vision loss. Reliable methods to identify patients at risk of progression to late stage AMD are lacking. Tan *et al*. used multimodal imaging, histological analysis and nano-analytical measurements to show that calcified nodules in the retina were associated with AMD progression. The authors found that these nodules were composed of hydroxyapatite and could be distinguished from other types of calcifications. The results suggest that multimodal imaging might help to guide therapeutic approaches and outcome measures in patients at risk of progressing to advanced AMD.